HHS Public Access

Author manuscript

Adv Mater. Author manuscript; available in PMC 2020 January 18.

Published in final edited form as:

Adv Mater. ; : e1803031. doi:10.1002/adma.201803031.

A Novel Top-Down Synthesis of Ultrathin Two-Dimensional Boron Nanosheets for Multi-modal Imaging-Guided Cancer Therapy

Dr. Xiaoyuan Ji[#],
School of Pharmaceutical Sciences (Shenzhen), Sun Yat-sen University, Guangzhou 510275, China

Center for Nanomedicine, Brigham and Women's Hospital, Harvard Medical School, Boston, Massachusetts 02115, United States

Dr. Na Kong[#],
Sir Run Run Shaw Hospital, Zhejiang University School of Medicine, Hangzhou, Zhejiang 310000, China

Dr. Junqing Wang[#],
Center for Nanomedicine, Brigham and Women's Hospital, Harvard Medical School, Boston, Massachusetts 02115, United States

Dr. Wenliang Li,
Center for Nanomedicine, Brigham and Women's Hospital, Harvard Medical School, Boston, Massachusetts 02115, United States

Dr. Yuling Xiao,
Center for Nanomedicine, Brigham and Women's Hospital, Harvard Medical School, Boston, Massachusetts 02115, United States

Silvia Tian Gan,
Center for Nanomedicine, Brigham and Women's Hospital, Harvard Medical School, Boston, Massachusetts 02115, United States

Dr. Ye Zhang,
Center for Nanomedicine, Brigham and Women's Hospital, Harvard Medical School, Boston, Massachusetts 02115, United States

Yujing Li,
Center for Nanomedicine, Brigham and Women's Hospital, Harvard Medical School, Boston, Massachusetts 02115, United States

Dr. Xiangrong Song,
Center for Nanomedicine, Brigham and Women's Hospital, Harvard Medical School, Boston, Massachusetts 02115, United States

Dr. Qingqing Xiong,

[*] meilin7@mail.sysu.edu.cn, hzhang@szu.edu.cn, jshi@bwh.harvard.edu.

Center for Nanomedicine, Brigham and Women's Hospital, Harvard Medical School, Boston, Massachusetts 02115, United States

Dr. Sanjun Shi,
Center for Nanomedicine, Brigham and Women's Hospital, Harvard Medical School, Boston, Massachusetts 02115, United States

Zhongjun Li,
Shenzhen Engineering Laboratory of Phosphorene and Optoelectronics, SZU-NUS Collaborative Innovation Center for Optoelectronic Science and Technology, and, Key Laboratory of Optoelectronic Devices and Systems of Ministry of Education and Guangdong Province Shenzhen University, Shenzhen 518060, China

Dr. Wei Tao,
Center for Nanomedicine, Brigham and Women's Hospital, Harvard Medical School, Boston, Massachusetts 02115, United States

Prof. Han Zhang[*],
Shenzhen Engineering Laboratory of Phosphorene and Optoelectronics, SZU-NUS Collaborative Innovation Center for Optoelectronic Science and Technology, and, Key Laboratory of Optoelectronic Devices and Systems of Ministry of Education and Guangdong Province Shenzhen University, Shenzhen 518060, China

Prof. Lin Mei[*], and
School of Pharmaceutical Sciences (Shenzhen), Sun Yat-sen University, Guangzhou 510275, China

Prof. Jinjun Shi[*]
Center for Nanomedicine, Brigham and Women's Hospital, Harvard Medical School, Boston, Massachusetts 02115, United States

[#] These authors contributed equally to this work.

Abstract

Single atom non-metal two-dimensional (2D) nanomaterials have shown considerable potential in cancer nanomedicines, owing to their intriguing properties and biocompatibility. Herein, ultrathin boron nanosheets (B NSs) were prepared through a novel top-down approach by coupling thermal oxidation etching and liquid exfoliation technologies, with controlled nanoscale thickness. Based on the PEGylated B NSs, a new photonic drug delivery platform was developed, which exhibited multiple promising features for cancer therapy and imaging, including (i) efficient NIR light to heat conversion with a high photothermal conversion efficiency of 42.5%, (ii) high drug-loading capacity and triggered drug release by NIR light and moderate acidic pH, (iii) strong accumulation at tumor sites, (iv) multimodal imaging properties (photoacoustic, photothermal and fluorescent imaging), and (v) complete tumor ablation and excellent biocompatibility. To the best of our knowledge, this is the first report on the top-down fabrication of ultrathin 2D B NSs by the combined thermal oxidation etching and liquid exfoliation, as well as their application as a multi-modal imaging-guided drug delivery platform. We also expect the newly prepared B NSs to provide a robust and useful 2D nanoplatform for various biomedical applications.

TOC

Ultrathin 2D boron (B)-based nanosheets (NSs) were fabricated through a novel top-down approach by coupling liquid exfoliating and thermal oxidation etching, and applied to photonic drug delivery for cancer therapy and imaging. The 2D B NS platform exhibits multiple promising features including efficient photothermal conversion, high drug loading, spatiotemporally controlled drug release, strong tumor accumulation, good biocompatibility, and significant potential of multimodal imaging guided-cancer treatment.

Keywords

Boron; Two-Dimensional nanosheet; Nanomedicine; Multi-modal imaging; Cancer therapy

Two-dimensional (2D) nanomaterials have received significant recognition in recent years owing to their outstanding physicochemical properties given rise to numerous potential applications, such as electronics, optoelectronics, and energy conversion and storage[1]. Moreover, some families of 2D nanomaterials have also been of interest in biomedical applications such as biosensing, tissue engineering, and cancer nanomedicine (*e.g.*, dug delivery, photothermal therapy, photodynamic therapy, and cancer imaging)[2], which mainly include the multi-atom-composed transition metal dichalcogenides, oxides, carbides, nitrides, or carbonitrides (MXenes)[3], and the single atom-composed non-metal/metal materials (*e.g.*, graphene, black phosphorus, and antimonene)[4]. Recently, elemental boron (B), closest to carbon (C) in the periodic table of elements, has drawn much attention with its high chemical stability, thermoelectricity, partial ionic bonding, and superconductivity[5]. Illuminated by the fabrication of graphene, several types of 2D B materials (*i.e.*, borophene) have been proposed theoretically[6]. On the experimental side, Wang *et al.* reported the discovery of a planar B36 cluster with sixfold symmetry and a perfect central hexagonal hole, providing the first experimental evidence that large-scale 2D B sheets are potentially viable[7]. Tai *et al.* reported the synthesis of ultrathin γ-B films (B28) on copper foils through chemical vapor deposition using a mixture of pure B and boron oxide (B_2O_3) powders as the B source, and hydrogen gas as the carrier gas[8]. Recently, a new 2D B sheet with single-atom thickness has been grown successfully on Ag (111) surfaces under ultrahigh-vacuum conditions and has attracted tremendous interest due to its extraordinary electronic, optical, thermal, and anisotropic mechanical properties[9]. However, these bottom-up methods for synthesis of B nanosheets (NSs) may encounter various disadvantages such as the necessary of vacuum environment, and separation from the base materials inevitably deteriorates the quality of the sheets and the yield. Therefore, developing a facile and robust approach for synthesis of B NSs with high-quality and high-yield will be particularly desirable for maximizing their potential applications.

Top-down strategies, including chemical exfoliation (*e.g.*, lithium intercalation and acid etching)[3a, 3c–f] and sonication-assisted liquid-phase exfoliation[4c, 4e, 10], have been proven to be efficient for the fabrication of 2D nanomaterials. In general, these exfoliation methods require the presence of layered structure in the bulk precursors, by which the weak Van der Waal's force among layers can be broken to form NSs. Unlike bulk graphite, BP and others with naturally layered structures, B exhibits more complex and diverse bulk structures due to

rich bonding configurations among B atoms, thus making it highly challenging to prepare ultrathin B NSs by direct exfoliation[11]. On the other hand, various etching technologies (*e.g.*, plasma etching, thermal oxidation etching, and acid etching)[12] have been developed to produce porous monolayer structures by breaking strong covalent bond in a layer of NSs, which have recently been used as high-performance energy-storage and hydrogen evolution reaction materials[13]. We thus hypothesized that the combination of exfoliation and etching technologies could lead to the robust generation of ultrathin 2D B NSs.

Herein, we designed a novel top-down method by coupling liquid exfoliating and thermal oxidation etching to prepare high-quality ultrathin 2D B NSs in large quantities (Scheme 1). The underlying mechanism of this method is that the B-B units on the thick layers (after the first liquid exfoliation) can be gradually oxidized in air at high temperature to form B_2O_3 which would then be dissolved into water by easily forming BO_3^{3-} with the second liquid exfoliation. Thus the size and thickness of bulk B will be decreased to the desired nanoscale (~100 nm of planar size and <5 nm of thickness). The resultant B NSs were then systematically evaluated as a new photonic drug delivery platform for cancer therapy and imaging. The B NSs were first modified with positively charged amine functionalized polyethylene glycol (PEG-NH_2) *via* electrostatic adsorption to further improve their biocompatibility and dispersibility. The PEGylated B NSs (B-PEG NSs) showed superior photothermal conversion efficiency (42.5%), which can be used as photothermal agents (PTAs) for cancer photothermal therapy (PTT) and have the probability for photothermal and photoacoustic (PA) imaging. In addition, the B-PEG NSs can also load chemotherapeutic agents such as doxorubicin (DOX) and imaging agents such as cyanine5.5 (Cy5.5) efficiently. Our *in vitro* and *in vivo* results demonstrated the potential of the B-PEG NSs for multi-model imaging-guided combinatorial cancer photothermal-chemotherapy.

In the first set of experiments, the B NSs were prepared from bulk B by the combination of liquid exfoliating processes and thermal oxidation etching. First, due to the high dispersibility of many NSs in N-methyl-2-pyrrolidone (NMP) and the high affinity between B and ethanol[14], we chose a mixture of NMP and ethanol (1:1 v/v) as the solvent for the liquid exfoliation of bulk B power into high dispersed B sheets solution. As shown in Figure 1a–b and 1i–j, the sheet structure of B was confirmed by transmission electron microscope (TEM) and atomic force microscope (AFM). The average size of B sheets was decreased from ~500 nm to ~250 nm, and the average thickness of B sheets was also decreased from ~50 nm to ~20 nm after liquid exfoliation in NMP and ethanol solution for 5 hrs. The decreases of lateral size and thickness may attribute the physical adsorbed and the fragmentary covalent bond grid among B sheets were broken by probe sonication in NMP and ethanol solution. High-resolution TEM (HRTEM) imaging and the corresponding fast fourier transform (FFT) diffraction pattern of the representative individual B sheet (inset of Figure 1e and 1f) confirm the crystalline nature of B sheets, showing a clear interference fringe with a *d*-spacing of 0.51 nm, corresponding to the (104) plane of a β-rhombohedral B structure[9a], which is displayed in Figure S1. The uniform lattice fringes shown in Figure 1f suggest that the crystalline state of the B sheets after liquid-phase exfoliation is pristine. X-ray photoelectron spectroscopy (XPS) further revealed the liquid exfoliation of B. As shown in Figure S2, there was only B element in the XPS survey spectra of bulk B and liquid exfoliated B sheets, demonstrating the high purity of B sheets after exfoliation. The high-

resolution XPS spectra of B (Figure 1m and 1n) show more detail of the liquid exfoliated B sheets. As the binding energy of B 1s peak in bulk B is ~189–190 eV (Figure 1m), the two low binding energy peaks (188.4 and 187.5 eV), which are slightly red-shifted compared to the bulk value, are most likely from B-B bonds in the pristine 2D B sheets (Figure 1n)[9b].

While 2D nanomaterials are defined as particles with one dimension confined to the nanometer length scale (<100 nm), the thinner of the thickness of 2D nanomaterials means the higher surface-to-mass ratio. The high surface-area-to-mass ratio of 2D nanomaterials with abundant anchoring points endows them with a high cargo-loading capacity for efficient drug delivery. The ultrathin thickness of 2D nanomaterials also enables them to respond rapidly to external stimuli (*e.g.*, light and pH), which has been of great interest for multi-responsive drug release and various optical therapy strategies (*e.g.*, PTT and photodynamic therapy)[4c–d, 10]. Even though some ultrathin 2D B NSs were observed by coupling the liquid exfoliation and high speed centrifugation (8000 rpm, 30 min), the yield of B NSs with the thickness of a few nanometers was very low (less than 1%). Therefore, new technologies are needed for preparing ultrathin 2D B NSs with high yield. One of the previous studies has already showed that although B has a high stability in air at room temperature, it is very easily oxidized by oxygen at high temperature, especially for 3D B structure. More interestingly, when the thickness of B sheet reach to one or a few atomic height, the oxidation of B only occur at the edges of the sheets, and the terrace of B remains almost intact[15]. The oxidized B layer, B_2O_3, can be easily exfoliated by dissolving them in water to form BO_3^{3-} with the help of probe sonication. According to the thermogravimetric analysis (TGA) and differential thermal analysis (DTA) of B shown in Figure S3, B would be oxidized to B_2O_3 when the temperature reached to 600–700 °C in air. Hence, the liquid exfoliated B sheets were continually exfoliated by coupling thermal oxidation etching at 650 °C and probe sonication in water. As shown in Figure 1c and 1k, after thermal oxidation, the average size of B sheets decreased to ~200 nm, and the average thickness of B sheets decreased to ~15 nm. The color of the photo image of thermal oxidized B sheets (inserted in Figure 1c) gives us the first evidence for successful thermal oxidation. The XPS spectrum further demonstrated the oxidation of B sheets. As shown in Figure S2, there was another element (O) shown in the XPS survey spectrum of B sheets after thermal oxidation etching. The high-resolution XPS spectrum of B (Figure 1o) gives us more details of thermal oxidation etching. Except the two low binding energy peaks (188.4 and 187.4 eV) attributed to B-B bonds in 2D B sheets, another strong peak at 191.7 eV was shown, which may ascribe to the oxidized B forming B-O bonds on the surface of B sheets caused by thermal oxidation[14a]. A much more complex crystalline structure shown in Figure 1g also demonstrates the formation of B_2O_3 on the surface of B sheets.

Then the ultrathin B NSs with the average size of ~110 nm and average thickness of ~3 nm were fabricated after further exfoliating the oxidized B_2O_3 layer in water (Figure 1d and 1l). The decreases of lateral size and thickness of B NSs can be mainly ascribed to the hydrolysis of B_2O_3 layer formed by thermal oxidation. HRTEM imaging (Figure 1h) and the corresponding FFT diffraction pattern of the representative individual B NSs (inset of Figure 1h) also demonstrate the crystalline nature of B NSs, and showed much more uniform and clear lattice fringes. As shown in high-resolution XPS spectra of B (Figure 1p), there were still some B-O bonds on the surface of B NSs caused by thermal oxidation etching, which

explains the negative zeta potential of −21.4 mV detected. The B-B binding energy peaks (188.2 and 187.0 eV), which are slightly redshifted compared with the liquid-exfoliated B sheets, further confirm the formation of ultrathin B NSs after exfoliating oxidized layers in water. Moreover, X-ray diffractometry (XRD) was used to analyze the crystal structure of prepared B NSs (Figure S4), consistent with JCPDS No. 01–089-2777. In addition, the size distribution of the ultrathin B NSs prepared by coupling thermal oxidation etching and liquid exfoliating was measured by dynamic light scattering (Figure S5), and the yield of the ultrathin B NSs was also enhanced to about 10% by weight, which is more than 10 times of that achieved through the liquid exfoliating in NMP and ethanol. Very recently, a precise and efficient method was reported to produce NSs of designed sizes through electrophoretic isolation of NSs in low melting agarose[16], which may be adopted to further obtain ultrathin B NSs with narrower size distribution.

In order to further improve the physiological stability and dispersibility of B NSs, PEG-NH_2 was modified on their surface *via* electrostatic adsorption. The amount of PEG-NH_2 that was coated on the surface of the B NSs was approximately 33.6% (w/w%) as measured by inductively coupled plasma-atomic emission spectrometry (ICP-AES). As shown in Figure 2a, B-PEG NSs showed negligible agglomeration after 24 h of incubation, and remarkably better stability and dispersibility in phosphate buffer saline (PBS) and cell culture medium compared to bare B NSs. The successful PEGylation of B NSs was confirmed by XPS (Figure 2b) and fourier transform infrared (FT-IR) spectra (Figure 2c). After PEGylation, there were two new peaks of C and N appeared in XPS spectrum of B-PEG NSs. For the FT-IR spectrum, the absorption bands at ~2900 cm^{-1} belong to the CH vibration and ~1250 cm^{-1} was contributed by C=O stretching vibrations in the PEG-NH_2 segment. Moreover, the elements, B (green), O (red), C (blue), and N (yellow), appeared in EDS mapping of B-PEG NSs (Figure 2h), further indicating the successful surface coating by PEG-NH_2. Following the similar process to coat PEG-NH_2, the fluorescence-functionalized PEG-NH_2 (Cy5.5-PEG-NH_2) was also modified on the surface of B NSs with the same method. The amount of Cy5.5-PEG-NH_2 coated on the B NSs surface was calculated to about 25.78% (w/w %) of the B-PEG/Cy5.5 NSs that was determined by the absorbance of Cy5.5-PEG-NH_2 (Figure S6).

In the second set of experiments, we explored the potential of their NIR-induced hyperthermia, including the UV-vis-NIR absorbance, photothermal conversion efficiency, and photothermal stability of B-PEG NSs. First, the UV-vis-NIR absorbance of B NSs before and after PEGylation all showed a broad and similar absorption band ranging from UV to NIR with varying concentration (Figure 2d, S7, and S8). Second, photothermal conversion efficiency was evaluated by exposing aqueous solutions of B-PEG NSs of different concentrations (0–200 μg/mL) to an 808-nm NIR laser at different power density (1–2 W/cm^2). Figure 2e, Figure S9 and S10 presented the temperature increase of B-PEG NSs of different concentrations and pure water during laser irradiation, which all showed a strong photothermal effect that was dependent on both the concentration and the power of the laser, in which the highest temperature change (ΔT_{max}) reached 37 °C after NIR laser (2 W/cm^2) irradiated for 5 min. In comparison, the temperature of pure water increased only 4 °C under the same conditions. However, without thermal oxidation etching and second liquid exfoliating in water, the B sheets after first liquid exfoliating in NMP and ethanol with

an average size of ~250 nm and the average thickness of ~20 nm has much less exposed surfaces to absorb NIR that led to the ΔT_{max} reaching only 11 °C under the same condition (Figure S11). The enhanced ΔT_{max} further confirmed the necessity of our strategy for the preparation of ultrathin B NSs.

The photothermal conversion efficiency (η) of B-PEG NSs was also measured by previously reported methods[4e, 10, 17]. The calculation details were described in Supporting Information. Calculated by Equation 5 (Supporting Information), the photothermal conversion efficiency of B-PEG NSs was 42.5% (Figure 2f), which is quite promising compared to most of the previously reported nanomaterial-based PTAs (Table S1). The high photothermal conversion efficiency suggests that B-PEG NSs can be developed as effective PTAs used for PTT of cancer. Besides, the photostability of B-PEG NSs was examined by exposing the B-PEG NSs solution to the NIR laser for five irradiation cycles. As shown in Figure 2g, there was negligible change of the photothermal effects during five cycles of heating and cooling processes at a higher power density of 2 W/cm^2, clearly suggesting the high photostability of B-PEG NSs. Moreover, we further incubated the developed B-PEG NSs in water for different number of days. The photothermal effects and UV-Vis-NIR absorbance spectra were tested using similar methods. As shown in Figure S12, no obvious changes occur in the photothermal effects and the UV-Vis-NIR absorbance spectra during the one month incubation in water, which also demonstrate a much higher stability against oxidation than that of BP NSs[4f].

Since 2D nanomaterials with large surface-area-to-volume ratio have been widely used as drug delivery platforms to interact with various drug molecules *via* π-π stacking and hydrophobic interactions[18], we further evaluated the potential of B-PEG NSs as drug carriers using DOX as the model drug. At first, B-PEG NSs were incubated with the different concentrations of DOX ranging from 200 to 1000 μg/mL for 24 h at room temperature. After repeated washing for three times, the drug-loading ratios of the B-PEG NSs were measured and calculated by UV-vis-NIR spectra (Figure 2i). With the increasing feeding ratio of DOX, the loading capacity of DOX increased almost linearly and reached a saturation level at a DOX/NSs feeding ratio of 5. As shown in Figure 2j, the saturation of DOX loading was reached to be 114% by weight. Nevertheless, the saturation loading capacity of DOX on the B sheets after first liquid exfoliating was calculated to be only ~21% (Figure S13), also demonstrating that the ultrathin B NSs with high surface-to-mass ratio have great potential in drug loading. Moreover, the fluorescence of DOX molecules loaded on the surface of B-PEG NSs could be partially quenched, indicating a strong interaction between the B-PEG NSs and DOX molecules (Figure S14). Stimuli-responsive drug release is a predominant property for drug delivery systems[19]. Previous studies have shown that most of NSs can release the loaded drugs in response to thermal and acidic stimuli[4c, 10]. The drug-release behavior of B-PEG NSs was further investigated under different treatments. As illustrated in Figure 2k, only ~8.3% of DOX was released from the B-PEG NSs at pH 7.4 after 24 h, while for pH 5.0, the amount of DOX released in 24 h reached to ~24.0%. The protonation of amino groups in DOX under acidic conditions will increase the hydrophilicity of DOX and decrease binding with NSs, which could be the main cause for the pH-responsive release of drugs. In consideration of the acidic tumor environment, the property of pH-responsive release of drugs will benefit the application of B-PEG/DOX NSs

for cancer therapy. In addition, the NIR-responsive release behavior of DOX was also evaluated. The released DOX over a span of 24 h drastically increased to ~41.4% and ~77.6% at pH 7.4 and 5.0, respectively, under laser irradiation for 5 min time interval. The NIR-induced drug release could be caused by NIR-induced local hyperthermia, which reduces the binding between B-PEG NSs and DOX.

Next, we detected the cytotoxicity of B-PEG NSs for cancer cells *in vitro*. Biocompatibility of B-PEG NSs is the prerequisite for their application as PTAs or drug carriers. Hence, the cytotoxicity of B-PEG NSs was examined in various cancer cells *in vitro*, including HeLa, PC3, MCF7, and A549. The cells' viability was evaluated by Alamarblue assay, presented in Figure 3a. After incubation with different concentrations of B-PEG NSs ranging from 25 to 500 μg/mL, there is no significant cytotoxicity observed in the four different cell lines even after incubation for 48 h with high concentrations. The release of lactate dehydrogenase (LDH) and reactive oxygen species (ROS), another two key toxicity signs of inorganic nanomaterials, were also tested. As shown in Figure S15, the LDH release and ROS concentration in B-PEG NSs treated cells were similar to the control group. All these results indicate the low cytotoxicity and high potential in biomedicine of B-PEG NSs. After confirming the photothermal conversion efficiency and biocompatibility of B-PEG NSs, the NIR-mediated photothermal cytotoxicity of the B-PEG NSs was further evaluated in two typical tumor cell lines, MCF7 and PC3. After incubated with B-PEG NSs for 4 h, the cells were exposed to an 808-nm NIR laser (1 W/cm^2) for 5 min. Cell viability was quantitatively detected and calculated through Alamarblue assays after incubation for another 24 h. Figure 3b notices a strong concentration-dependent cytotoxicity after laser irradiation in cell lines. More than 85% of MCF7 and up to 90% of PC3 cells were effectively killed by B-PEG NSs under laser irradiation at a concentration of 200 μg/mL. Laser scanning confocal microscopy (LSCM) images provide the similar results through co-staining cells with calcein AM (live cells, green fluorescence) and propidium iodide (PI, dead cells, red fluorescence) after the PTT treatment (Figure 3d), which further demonstrate the good PTT efficiency of the B-PEG NSs in cancer cells.

The combinatorial PTT and chemotherapy of B-PEG/DOX NSs was investigated in two different cell lines (MCF7 and PC3). First, cells were incubated with free DOX, B-PEG, or B-PEG/DOX, in either the absence or presence of NIR irradiation (808 nm, 1 W cm^{-2}, 5 min) at increasing concentrations. Similar to Figure 3a, negligible toxicity was observed from the cells treated with B-PEG NSs alone, while a dose-dependent toxicity was observed in the B-PEG NSs treated with irradiation of NIR (Figure 3c). Cells treated with B-PEG/DOX NSs also showed a dosage-dependent cell death, but a bit lower than that of free DOX at the same DOX concentration. Notably, when the B-PEG NSs were combined with both DOX loading and NIR laser irradiation, over 95% of the cells died at a DOX concentration of 100 μg/mL. Similar results were obtained with PC3 cells (Figure S16), demonstrating the high efficacy of combined chemo-photothermal therapy strategy based on B-PEG/DOX NSs.

Given these exciting results *in vitro*, the possibilities of using the B-PEG NSs as a photonic delivery platform for *in vivo* application was further carried out. To do this, we first established the MCF7 xenograft tumor model. The biodistribution of Cy5.5-labeled B-PEG

NSs and tumor accumulation after *i.v.* injection at different time points were tested *via* a whole-animal NIR imaging approach. As shown in Figure 4a, at 24 h post-injection, free Cy 5.5 did not accumulate efficiently in the tumor due to its short blood circulation time. In contrast, B-PEG/Cy5.5 NSs showed significantly higher level of drug accumulation in the tumor. This high tumor accumulation of NSs could be generally attributed to the enhanced permeability and retention (EPR) effect that has been widely reported but is still not comprehensively understood[20]. In addition to the leaky vasculature allowing passive extravasation of nanomedicine into tumor tissues, several other mechanisms have recently been proposed[21]. For example, Leong et al. reported that certain nanomaterials with specific characteristics (e.g., small size, appropriate density, negatively charged surface, etc.) were able to induce the opening of the paracellular route of the vascular barrier through their interaction with vascular endothelial cadherins (VE-cadherins). This nanomaterial-induced endothelial leakiness (NanoEL) can also allow higher tumor accumulation of nanomedicine. Strong fluorescence signals were detected mainly in the tumor and in some organs such as liver, lung, and kidney. The accumulation of these NSs in liver could be attributed to the absorption of the mononuclear phagocyte system; those accumulated in kidney may be caused by possible renal excretion, and those accumulated in lung may be related with mechanical retention of large-sized NSs. The high accumulation of NSs in tumor due to the EPR effect also indicates promising potential for systematic delivery in cancer therapy (Figure 4b). In addition, the extended circulation time verified through pharmacokinetic studies was also in good agreement with the biodistribution results (Figure S17).

Recently, PA imaging has become one of the most promising biophotonic diagnostic modalities for facilitating imaging-guided cancer theranostics, due to deep detection, depth-resolved 3D imaging, high sensitivity, spatial resolution, and image contrast[22]. Since as-prepared B-PEG NSs exhibit excellent photothermal performance, the potential of B-PEG NSs as a PA agent was evaluated *in vitro* and *in vivo*. Figure 4c presents a strong concentration-dependent PA signal at 780 nm wavelengths. Moreover, a good linearity of the PA signal as a function of B-PEG NSs concentration was observed in Figure 4e. All these results showed that B-PEG NSs will be a good PA agent for facilitating imaging-guided cancer therapy. For PA imaging *in vivo*, the MCF7 tumor-bearing mice were intravenously injected for B-PEG NSs. After injection, the signal was recorded on the PA instrument at different time points (0, 12, and 24 h). Very strong PA signals were observed in Figure 4d at the tumor sites 12 h and 24 h after *i.v.* injection of B-PEG NSs through *in vivo* ultrasound and PA images at 780 nm wavelengths. In addition, the quantitative analysis of each PA signal further demonstrated the potential of B-PEG NSs as a PA agent for cancer imaging (Figure 4f), as well as imaging-guided drug delivery and patient selection.

After confirming the potential fluorescence and PA dual-modal imaging of the B-based delivery platforms, we carried out an antitumor study to validate the potential of B-PEG/DOX NSs for *in vivo* combinatorial cancer therapy. MCF7 breast tumor-bearing mice were then divided into five groups. Each group was treated as follows. Group 1: saline (control), Group 2: DOX (free drug), Group 3: B-PEG/DOX NSs (drug delivery), Group 4: B-PEG NSs + NIR (PTT), and Group 5: B-PEG/DOX NSs (chemo-photothermal combined therapy). The intravenously injected dose of DOX and B-PEG NSs were 6 mg/kg and 5.3 mg/kg in all corresponding groups, respectively. Groups 4 and 5 were irradiated with NIR

laser (1 W cm^{-2}, 808 nm) for 10 min at 12 h post-injection. An IR thermal camera was used to record the temperature changes in different groups (Figure 4g and 4h). Figure 4h shows that the tumor temperature in Groups 1–3 without NIR irradiation treatment remained stable (~35–36 °C), whereas the tumor temperature in the Group 4 and 5 were increased by ~20 °C to over 55 °C after the same irradiation period. After different treatments, the volumes of tumors were calculated on the basis of their length and width measured by a digital caliper every 2 day (Figure 4i). As expected, compared with saline, Groups 2–5 all showed decreasing tumor growth in mice. Better therapeutic effects were observed in Groups 3 (drug delivery) and 4 (PTT) than in Group 2 (free DOX), indicating the potential application of B-PEG NSs as drug delivery platforms and PTAs. Notably, Group 5 showed extremely high inhibition of tumor growth, where tumors even disappeared without recurrence in all five mice of this group, indicating the remarkably enhanced therapeutic effect of chemo-photothermal combined treatment. Digital photos of tumors excised from representative mice also reflect the excellent therapeutic effect of the B-PEG/DOX NSs (Figure 4j). No obvious side effects were noted in these groups, such as abnormal weight loss (Figure 4k), perturbations in eating, drinking, activity, or neurological issues.

In the final set of experiments, the potential *in vivo* toxicity of B-PEG NSs was evaluated. Healthy mice were intravenously injected with PBS or B-PEG NSs through the tail vein. Serum samples were collected at 2 and 24 h post injection for immune analysis. The levels of TNF-α, IL-6, IFN-γ, and IL-12+P40 were similar to those in the PBS control group (Figure 5a–d), indicating that B-PEG NSs did not induce obvious cytokine response. For the hematology assay and histology examination, the blood of healthy mice intravenously injected with PBS or B-PEG NSs was collected at 1, 7, and 14 d post-injection. Various serum biochemical parameters including alkaline phosphatase (ALP), aspartate aminotransferase (AST), urea nitrogen (BUN), and alanine aminotransferase (ALT) were measured (Figure 5e–h). For the blood routine examination, hemoglobin (HGB), white blood cells (WBC), red blood cells (RBC), mean corpuscular volume (MCV), mean corpuscular hemoglobin concentration (MCHC), platelet (PLT), mean corpuscular hemoglobin (MCH), hematocrit (HCT), creatinine (Cr), neutrophil (NEU), lymphocyte (LYM), and mean platelet volume (MPV) counts were measured (Figure 5i–t). Compared with the control group, there is no statistically significant difference of the NSs-treated groups with PBS-treated groups in all the parameters. These results demonstrate that the B-PEG NSs do not cause obvious infection and inflammation in the treated mice. Moreover, no noticeable signal of inflammation or tissue damage was observed in major organs including heart, liver, lung, spleen, and kidney (Figure 5w).

In conclusion, we reported for the first time a new top-down method to prepare 2D B NSs with high-quality and high-yield, as well as the application of B-PEG NSs as a photonic drug delivery platform. By coupling liquid exfoliating and thermal oxidation etching processes, ultrathin B NSs were fabricated with average size of ~110 nm and average thickness of ~3 nm. The B-PEG NSs exhibited strong NIR absorption and efficient generation of hyperthermia upon laser irradiation with a high photothermal conversion efficiency of 42.5%. Using DOX as a model drug, the B-PEG NSs also showed high drug loading capacity and multi-responsive (*i.e.*, pH-/photo-responsive) drug release properties. Systematic *in vitro* and *in vivo* evaluation demonstrated highly effective combinatorial

antitumor efficacy of the DOX-loaded B-PEG NSs, and their potential for multi-modal fluorescence, PA, and photothermal imaging. Preliminary toxicity studies also indicated the biocompatibility of these NSs without inducing cytokine response and tissue injury, while long-term toxicity and metabolism will still be needed to further validate their biosafety. Compared with multi-atom-composed 2D nanomaterials such as MXenes[3], single atom non-metal B NSs may be more biocompatible for biomedical applications due to the potential benefits of B to human beings[23]. Meanwhile, B NSs show a great stability in air and water at room temperature[9], as compared to black phosphorus[4e]. It is thus expected that the novel top-down synthesis of ultrathin 2D B NSs could widely expand their potential application in the fields of nanomedicines, electronics, and others.

Supplementary Material

Refer to Web version on PubMed Central for supplementary material.

Acknowledgements

This study is supported by the US National Institutes of Health (NIH) CA200900; Natural Science Foundation of Guangdong Province 2016A030310023; National Natural Science Foundation of China (81771966); Guangdong Natural Science Funds for Distinguished Young Scholar (2014A030306036); China Postdoctoral Science Foundation 2016M600676; and Tsinghua Scholarship for Overseas Graduate Studies 2013159; Science, Technology & Innovation Commission of Shenzhen Municipality (JCYJ20160531195129079).

References

[1]. a) Wang H, Yuan H, Hong SS, Li Y, Cui Y, Chem. Soc. Rev 2015, 44, 2664–2680 [PubMed: 25474482] b) Wang QH, Kalantar-Zadeh K, Kis A, Coleman JN, Strano MS, Nat. Nanotechnol 2012, 7, 699–712 [PubMed: 23132225] c) Jariwala D, Sangwan VK, Lauhon LJ, Marks TJ, Hersam MC, ACS Nano 2014, 8, 1102–1120 [PubMed: 24476095] d) Li H, Shi Y, Chiu M-H, Li L-J, Nano Energy 2015, 18, 293–305e) Ryder CR, Wood JD, Wells SA, Hersam MC, ACS Nano 2016, 10, 3900–3917. [PubMed: 27018800]

[2]. a) Chimene D, Alge DL, Gaharwar AK, Adv. Mater 2015, 27, 7261–7284 [PubMed: 26459239] b) Chen Y, Wu Y, Sun B, Liu S, Liu H, Small 2017, 13, 1603446c) Li H, Wu J, Yin Z, Zhang H, Acc. Chem. Res 2014, 47, 1067–1075. [PubMed: 24697842]

[3]. a) Zhu X, Ji X, Kong N, Chen Y, Mahmoudi M, Xu X, Ding L, Tao W, Cai T, Li Y, Gan T, Barrett A, Bharwani Z, Chen H, Farokhzad OC, ACS Nano 2018, 12, 2922–2938 [PubMed: 29406760] b) Cheng L, Liu J, Gu X, Gong H, Shi X, Liu T, Wang C, Wang X, Liu G, Xing H, Bu W, Sun B, Liu Z, Adv. Mater 2014, 26, 1886–1893 [PubMed: 24375758] c) Chou SS, Kaehr B, Kim J, Foley BM, De M, Hopkins PE, Huang J, Brinker CJ, Dravid VP, Angew. Chem. Int. Ed 2013, 52, 4160–4164d) Liu T, Wang C, Gu X, Gong H, Cheng L, Shi X, Feng L, Sun B, Liu Z, Adv. Mater 2014, 26, 3433–3440 [PubMed: 24677423] e) Lin H, Gao S, Dai C, Chen Y, Shi J, J. Am. Chem. Soc 2017, 139, 16235–16247 [PubMed: 29063760] f) Lin H, Wang X, Yu L, Chen Y, Shi J, Nano Lett 2017, 17, 384–391 [PubMed: 28026960] g) Lin H, Wang Y, Gao S, Chen Y, Shi J, Adv. Mater 2018, 30, 1703284h) Wang S, Chen Y, Li X, Gao W, Zhang L, Liu J, Zheng Y, Chen H, Shi J, Adv. Mater 2015, 27, 7117–7122 [PubMed: 26447460] i) Chen Y, Ye D, Wu M, Chen H, Zhang L, Shi J, Wang L, Adv. Mater 2014, 26, 7019–7026 [PubMed: 25156250] j) Wang S, Li X, Chen Y, Cai X, Yao H, Gao W, Zheng Y, An X, Shi J, Chen H, Adv. Mater 2015, 27, 2775–2782. [PubMed: 25821185]

[4]. a) Wang H, Yang X, Shao W, Chen S, Xie J, Zhang X, Wang J, Xie Y, J. Am. Chem. Soc 2015, 137, 11376–11382 [PubMed: 26284535] b) Qian X, Gu Z, Chen Y, Mater. Horiz 2017, 4, 800–816c) Tao W, Zhu X, Yu X, Zeng X, Xiao Q, Zhang X, Ji X, Wang X, Shi J, Zhang H, Mei L, Adv. Mater 2017, 29, 1603276d) Tao W, Ji X, Xu X, Islam MA, Li Z, Chen S, Saw PE, Zhang H, Bharwani Z, Guo Z, Shi J, Farokhzad OC, Angew. Chem. Int. Ed 2017, 56, 11896–11900e) Shao

J, Xie H, Huang H, Li Z, Sun Z, Xu Y, Xiao Q, Yu X-F, Zhao Y, Zhang H, Wang H, Chu PK, Nat. Commun, 2016, 7, 12967. [PubMed: 27686999]

[5]. a) Albert B, Hillebrecht H, Angew. Chem. Int. Ed 2009, 48, 8640–8668b) Ogitsu T, Schwegler E, Galli G, Chem. Rev 2013, 113, 3425–3449. [PubMed: 23472640]

[6]. a) Wang X, Tian J, Yang T, Bao L, Hui C, Liu F, Shen C, Gu C, Xu N, Gao H, Adv. Mater 2007, 19, 4480–4485b) Zhai H-J, Zhao Y-F, Li W-L, Chen Q, Bai H, Hu H-S, Piazza ZA, Tian W-J, Lu H-G, Wu Y-B, Mu Y-W, Wei G-F, Liu Z-P, Li J, Li S-D, Wang L-S, Nat. Chem 2014, 6, 727–731 [PubMed: 25054944] c) Chen Q, Li W-L, Zhao Y-F, Zhang S-Y, Hu H-S, Bai HH-R, Tian W-J, Lu H-G, Zhai H-J, Li S-D, Li J, Wang L-S, ACS Nano 2015, 9, 754–760. [PubMed: 25517915]

[7]. Piazza ZA, Hu H-S, Li W-L, Zhao Y-F, Li J, Wang L-S, Nat. Commun 2014, 5, 3113. [PubMed: 24445427]

[8]. Tai G, Hu T, Zhou Y, Wang X, Kong J, Zeng T, You Y, Wang Q, Angew. Chem. Int. Ed 2015, 54, 15473–15477.

[9]. a) Mannix AJ, Zhou X-F, Kiraly B, Wood JD, Alducin D, Myers BD, Liu X, Fisher BL, Santiago U, Guest JR, Yacaman MJ, Ponce A, Oganov AR, Hersam MC, Guisinger NP, Science 2015, 350, 1513–1516 [PubMed: 26680195] b) Feng B, Zhang J, Zhong Q, Li W, Li S, Li H, Cheng P, Meng S, Chen L, Wu K, Nat. Chem 2016, 8, 564–569.

[10]. Liu Y, Ji X, Liu J, Tong WWL, Askhatova D, Shi J, Adv. Funct. Mater 2017, 27, 1703261. [PubMed: 29290753]

[11]. Sun X, Liu X, Yin J, Yu J, Li Y, Hang Y, Zhou X, Yu M, Li J, Tai G, Guo W, Adv. Funct. Mater 2017, 27, 1603300.

[12]. a) Li H, Tan Y, Liu P, Guo C, Luo M, Han J, Lin T, Huang F, Chen M, Adv. Mater 2016, 28, 8945–8949 [PubMed: 27561130] b) Surwade SP, Smirnov SN, Vlassiouk IV, Unocic RR, Veith GM, Dai S, Mahurin SM, Nat. Nanotechnol 2015, 10, 459–464 [PubMed: 25799521] c) Wu J, Peng J, Yu Z, Zhou Y, Guo Y, Li Z, Lin Y, Ruan K, Wu C, Xie Y, J. Am. Chem. Soc 2018, 140, 493–498 [PubMed: 29202228] d) Zhu Y, Murali S, Stoller MD, Ganesh KJ, Cai W, Ferreira PJ, Pirkle A, Wallace RM, Cychosz KA, Thommes M, Su D, Stach EA, Ruoff RS, Science 2011, 332, 1537–1541 [PubMed: 21566159] e) Niu P, Zhang L, Liu G, Cheng H-M, Adv. Funct. Mater 2012, 22, 4763–4770.

[13]. a) Kang J, Sangwan VK, Wood JD, Hersam MC, Acc. Chem. Res 2017, 50, 943–951 [PubMed: 28240855] b) Zhu Y, Murali S, Stoller MD, Ganesh KJ, Cai W, Ferreira PJ, Pirkle A, Wallace RM, Cychosz KA, Thommes M, Science 2011, 332, 1537. [PubMed: 21566159]

[14]. a) Kang J, Wood JD, Wells SA, Lee J-H, Liu X, Chen K-S, Hersam MC, ACS Nano 2015, 9, 3596–3604 [PubMed: 25785299] b) Nagarajan V, Chandiramouli R, Comput. Theor.Chem 2017, 1105, 52–60.

[15]. Wan B, Zhou Q, Zhang J, Wang Y, Yang B, Lv W, Zhang B, Zeng Z, Chen Q, Wang J, Wang W, Wen F, Xiang J, Xu B, Zhao Z, Tian Y, Liu Z, Adv. Electron. Mater 2018, 4, 1700455

[16]. Tay DMY, Lin LB, Tan ESL, Loh KP, Leong DT, Adv. Funct. Mater, 2018, 1801622.

[17]. a) Roper DK, Ahn W, Hoepfner M, J.Phys. Chem. C 2007, 111, 3636–3641b) Liu Y, Ji X, Liu J, Tong WWL, Askhatova D, Shi J, Adv. Funct. Mater 2017, 27, 1703261 [PubMed: 29290753] c) Jiang Y, Li J, Zhen X, Xie C, Pu K, Adv. Mater 2018, 30, 1705980.

[18]. Yang K, Feng L, Shi X, Liu Z, Chem.Soc. Rev 2013, 42, 530–547. [PubMed: 23059655]

[19]. a) Wang C, Wang J, Zhang X, Yu S, Wen D, Hu Q, Ye Y, Bomba H, Hu X, Liu Z, Sci. Transl. Med 2018, 10, eaan3682 [PubMed: 29467299] b) Chen Z, Wang J, Sun W, Archibong E, Kahkoska AR, Zhang X, Lu Y, Ligler FS, Buse JB, Gu Z, Nat. Chem. Biol 2018, 14, 86–93 [PubMed: 29083418] c) Apsite I, Stoychev G, Zhang W, Jehnichen D, Xie J, Ionov L, Biomacromolecules 2017, 18, 3178–3184 [PubMed: 28840711] d) Liang C, Xu L, Song G, Liu Z, Chem. Soc. Rev 2016, 45, 6250–6269 [PubMed: 27333329] e) Ye Y, Yu J, Wen D, Kahkoska AR, Gu Z, Adv. Drug Deliver. Rev 2018, DOI: j.addr.2018.01.015f) Zhang F, Ni Q, Jacobson O, Cheng S, Liao A, Wang Z, He Z, Yu G, Song J, Ma Y, Niu G, Zhang L, Zhu G, Chen X, Angew. Chem. Int. Ed 2018, DOI: 10.1002/anie.201801984g) Fan W, Yung BC, Chen X, Angew. Chem. Int. Ed 2018, DOI: 10.1002/anie.201800594.

[20]. a) Shi J, Kantoff PW, Wooster R, Farokhzad OC, Nat. Rev. Cancer 2016, 17, 20–37 [PubMed: 27834398] b) Rosenblum D, Joshi N, Tao W, Karp JM, Peer D, Nature Communications 2018, 9,

1410c) Chen H, Zhang W, Zhu G, Xie J, Chen X, Nat. Rev. Materials 2017, 2, 17024; Wang S, Huang P, Chen X, Adv. Mater 2016, 28, 7340–7364. [PubMed: 29075517]

[21]. a) Matsumoto Y, Nichols JW, Toh K, Nomoto T, Cabral H, Miura Y, Christie RJ, Yamada N, Ogura T, Kano MR, Matsumura Y, Nishiyama N, Yamasoba T, Bae YH, Kataoka K, Nat. Nanotechnol 2016, 11, 533–538 [PubMed: 26878143] b) Wang J, Zhang L, Peng F, Shi X, Leong DT, Chem. Mater 2018, DOI: 10.1021/acs.chemmater.8b00840c) Setyawati MI, Mochalin VN, Leong DT, ACS Nano 2016, 10, 1170–1181 [PubMed: 26643115] d) Tay CY, Setyawati MI, Leong DT, ACS Nano 2017, 11, 2764–2772 [PubMed: 28287706] e) Setyawati MI, Tay CY, Bay BH, Leong DT, ACS Nano 2017, 11, 5020–5030 [PubMed: 28422481] f) Setyawati MI, Tay CY, Docter D, Stauber RH, Leong DT, Chem. Soc. Rev 2015, 44, 8174–8199 [PubMed: 26239875] g) Setyawati MI, Tay CY, Chia SL, Goh SL, Fang W, Neo MJ, Chong HC, Tan SM, Loo SC, Ng KW, Xie JP, Ong CN, Tan NS, Leong DT, Nat. Commun 2013, 4, 1673. [PubMed: 23575677]

[22]. a) Wang LV, Hu S, Science 2012, 335, 1458–1462 [PubMed: 22442475] b) Pu K, Shuhendler AJ, Jokerst JV, Mei J, Gambhir SS, Bao Z, Rao J, Nat. Nanotechnol 2014, 9, 233–239 [PubMed: 24463363] c) Lee DY, Kim JY, Lee Y, Lee S, Miao W, Kim HS, Min J-J, Jon S, Angew. Chem. Int. Ed 2017, 56, 13684– 13688.d) Pu K, Zhen X, Zhang J, Huang J, Xie C, Miao Q, Angew. Chem. Int. Ed 2018, DOI: 10.1002/anie.201803321.

[23]. Nielsen FH, Plant Soil 1997, 193, 199–208.

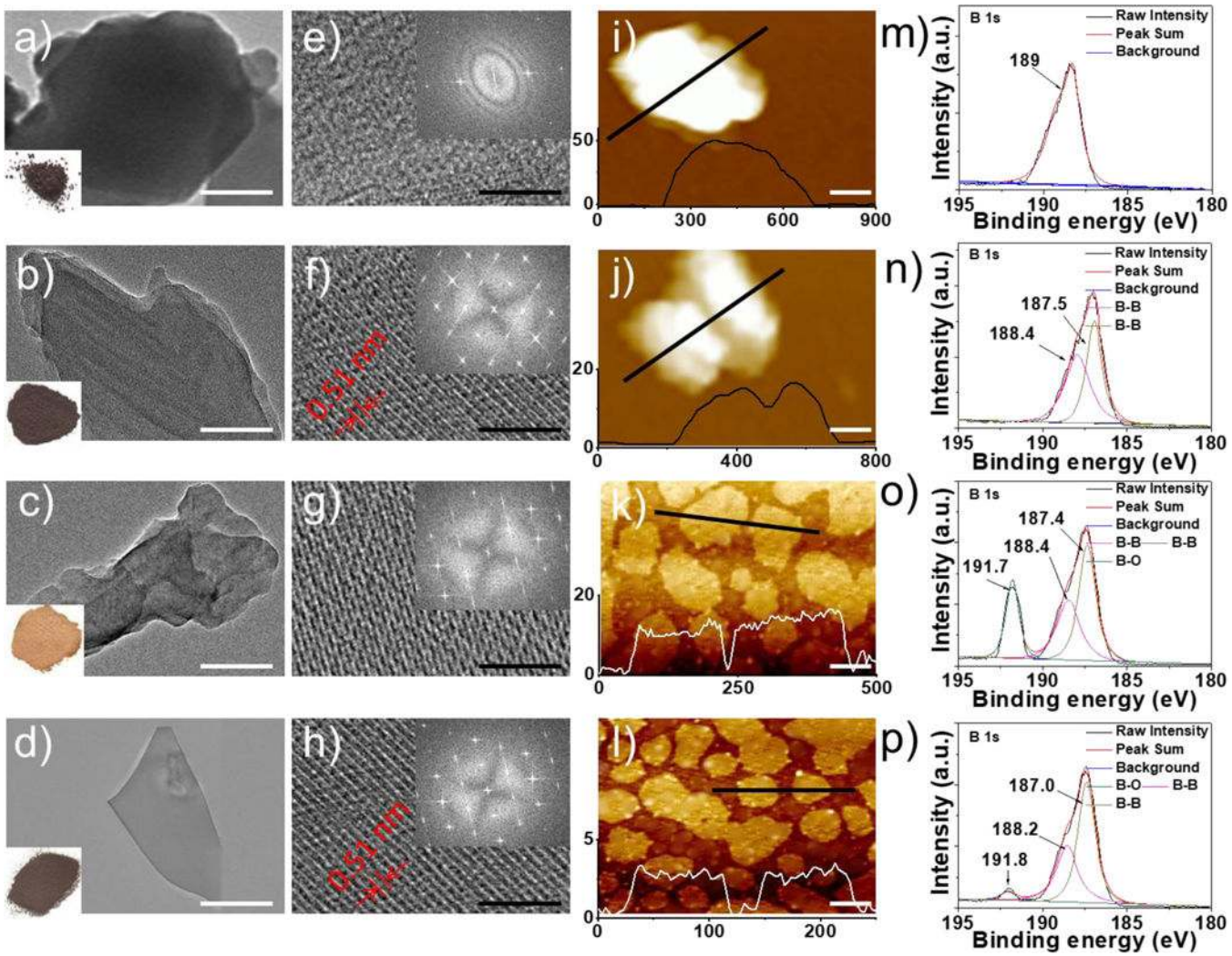

Figure 1.

Preparation and Characterization of ultrathin 2D B NSs. a–d) TEM image (insert: photo image), e–h) HRTEM image (insert: FFT diffraction patterns), i–l) AFM image, and m–p) XPS spectra of B after dispersed in NMP and ethanol solution, liquid exfoliated B sheets in NMP and ethanol solution, thermal oxidation etched B sheets, and liquid exfoliated B NSs in water, respectively. The white and black scale bars represent 100 nm and 5 nm, respectively.

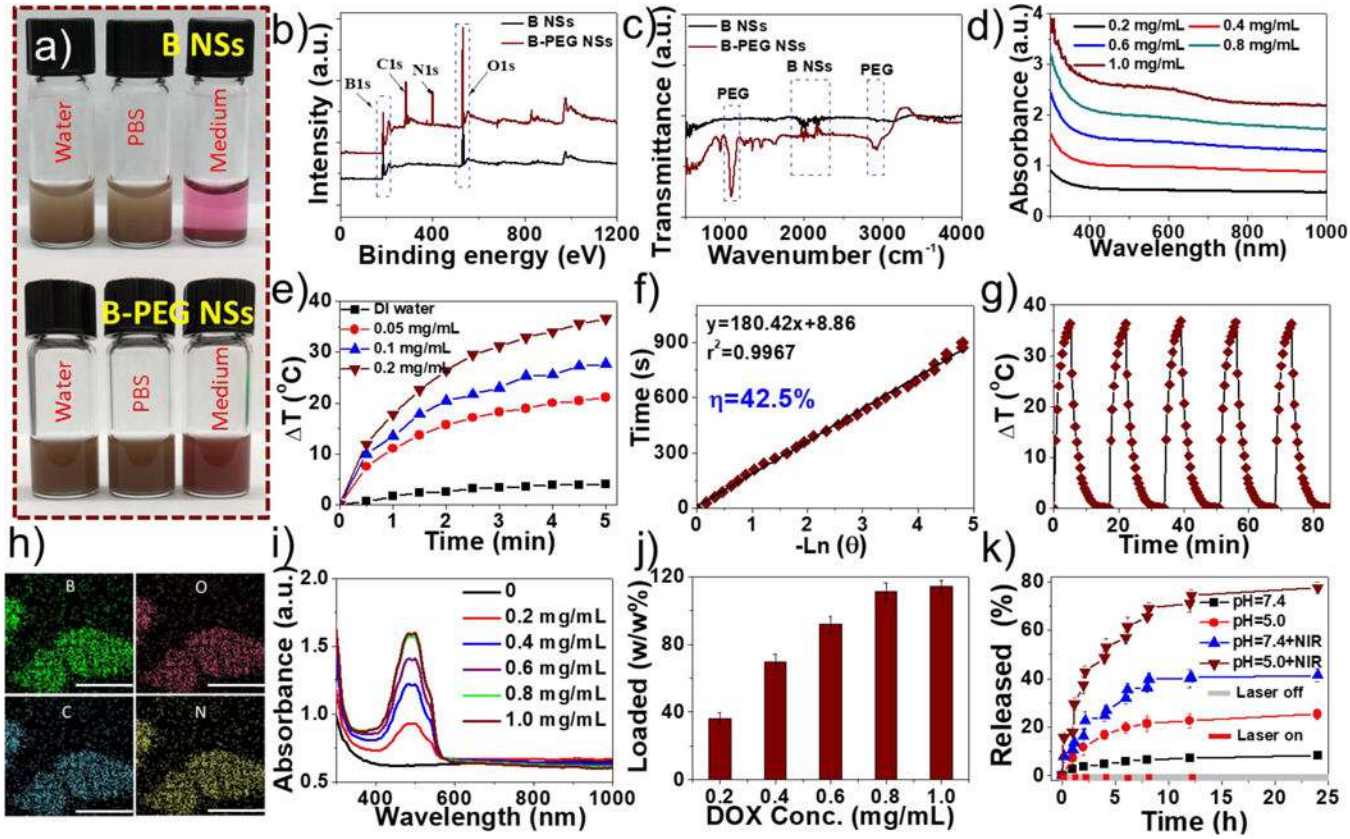

Figure 2.

Characterization of B-based NSs for photonic drug delivery platform. a) Dispersibility, b) XPS spectra, c) FTIR spectra of B-based NSs. d) UV-vis-NIR absorbance spectra of B-PEG NSs. e) Photothermal heating curves of DI water and B-PEG NSs at different concentrations under 808 nm laser irradiation (2 W/cm^2) for 5 min. f) Linear relationship between time and -ln θ calculated from cooling period after the laser was turned off. g) Photothermal conversion stability of B-PEG NSs. The laser was turned on for 5 min and then turned off for each cycle. The concentration of B-PEG NSs is 200 μg/mL and the laser power density is 2 W/cm^2. h) STEM-EDS mapping images of B-PEG/DOX NSs. The scale bars represent 100 nm. i) UV-vis-NIR absorbance of B-PEG/DOX NSs at different DOX feeding concentrations after the removal of excess free DOX. j) DOX loading capacities on B-PEG NSs (w/w %) with increasing DOX feeding concentrations. k) Release profiles of DOX at different pHs with or without 808-nm NIR laser (1 W/cm^2).

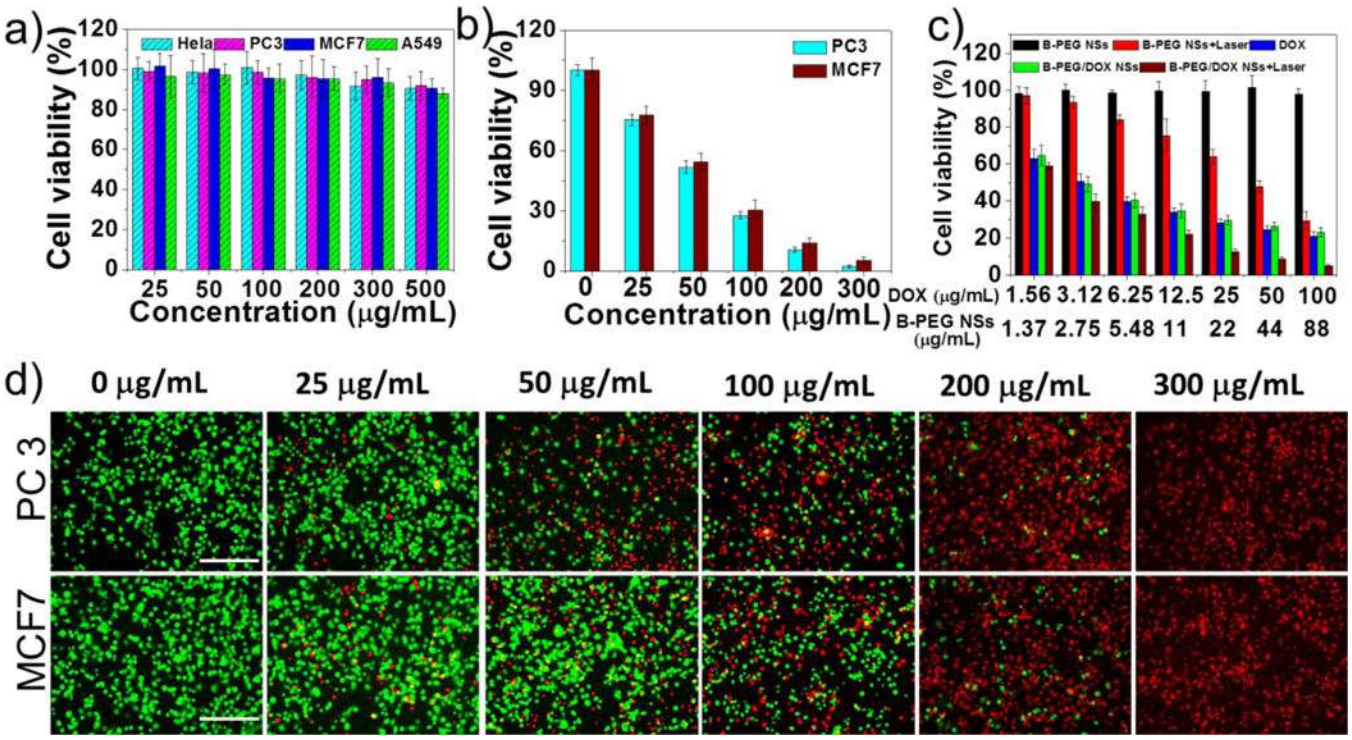

Figure 3.

Cell experiments. a) Relative viability of Hela, PC3, MCF7, and A549 cells after incubation with B-PEG NSs (concentrations of 25, 50, 100, 200, 300 and 500 μg/mL) for 48 h. b) Relative viability of PC3 and MCF7 cells after incubation with B-PEG NSs (concentrations of 0, 25, 50, 100, 200, and 300 μg/mL) for 4 h after irradiation with 808 nm laser (1W/cm^2) for 10 min. c) Cell viability of MCF7 cells after treatment with various groups. d) Corresponding laser scanning confocal microscopy (scale bars, 200 μm for all panels) of PC3 and MCF7 cells stained with calcein AM (live cells, green fluorescence) and PI (dead cells, red fluorescence).

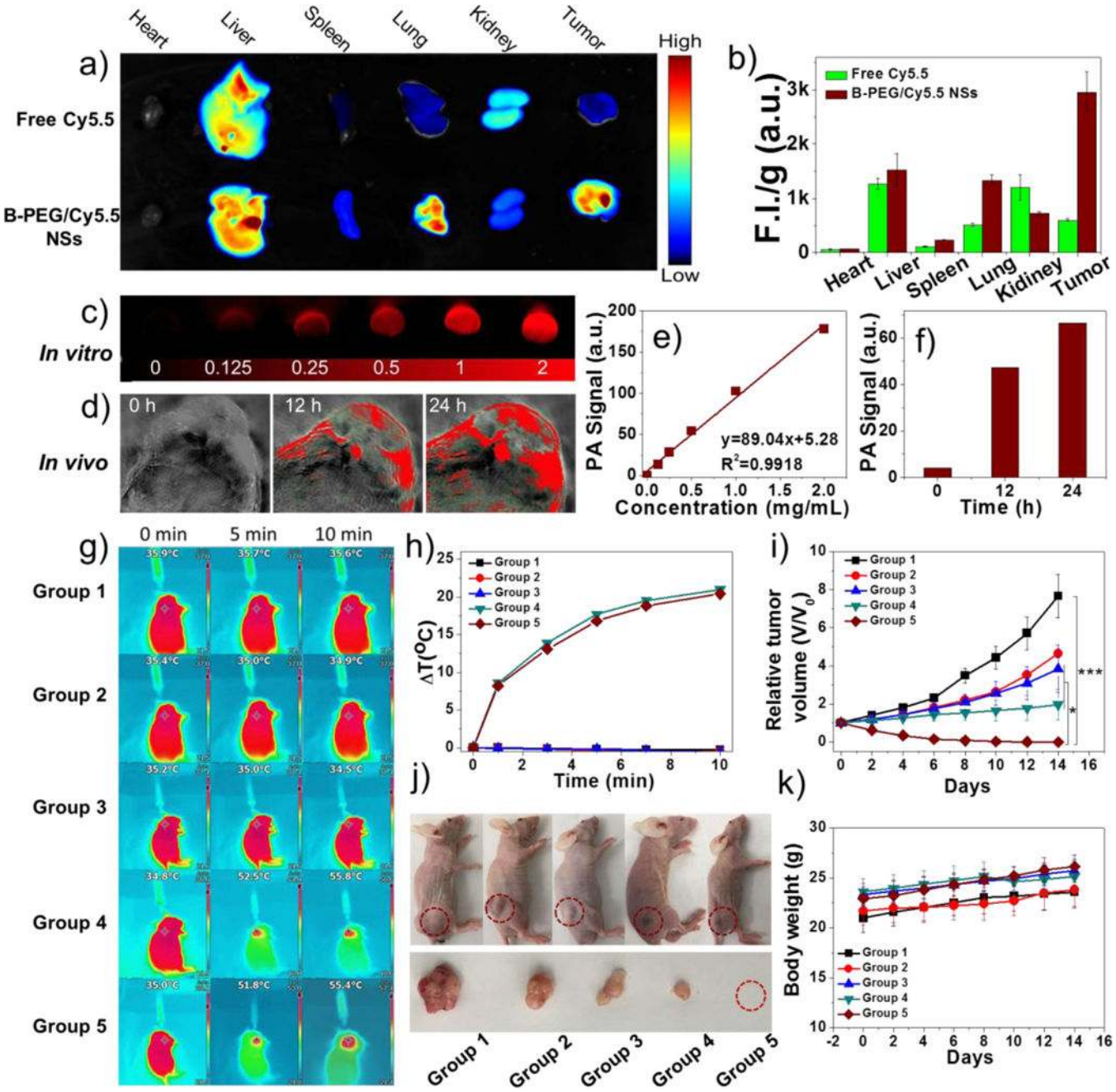

Figure 4.

In vivo imaging, biodistribution and combined cancer therapy effect of B-based NSs. a) *Ex vivo* fluorescence images of the tumor and major organs at 24 h post-injection. b) Semi-quantitative biodistribution of free Cy 5.5 or Cy5.5-labelled B-PEG NSs in nude mice detected by the average fluorescence intensity of tumors and major organs per gram. c) *In vitro* PA images of B-PEG NSs as a function of concentration (0, 125, 250, 500, 1000, and 2000 μg/mL). d) PA images of the tumor site at different time intervals (1, 12, 24 h) post-injection. e) PA values of B-PEG NSs as a function of concentration (0, 125, 250, 500, 1000, and 2000 μg/mL). f) Quantitative analysis of PA values in Figure 4d. g) Infrared

thermographic maps and h) Time-dependent temperature changes in the MCF7 tumor-bearing nude mice after different treatments. i) Growth curves of MCF7 tumor bearing nude mice after different treatments. j) Digital photos of representative tumors in different groups after 14 days of treatment. k) Body weight of mice in different groups during treatment. Group 1: saline; Group 2: DOX; Group 3: B-PEG/DOX NSs; Group 4: B-PEG NSs + NIR (808 nm, 1 W cm^{-2}, 10 min); Group 5: B-PEG/DOX NSs + NIR (808 nm, 1 W cm^{-2}, 10 min).

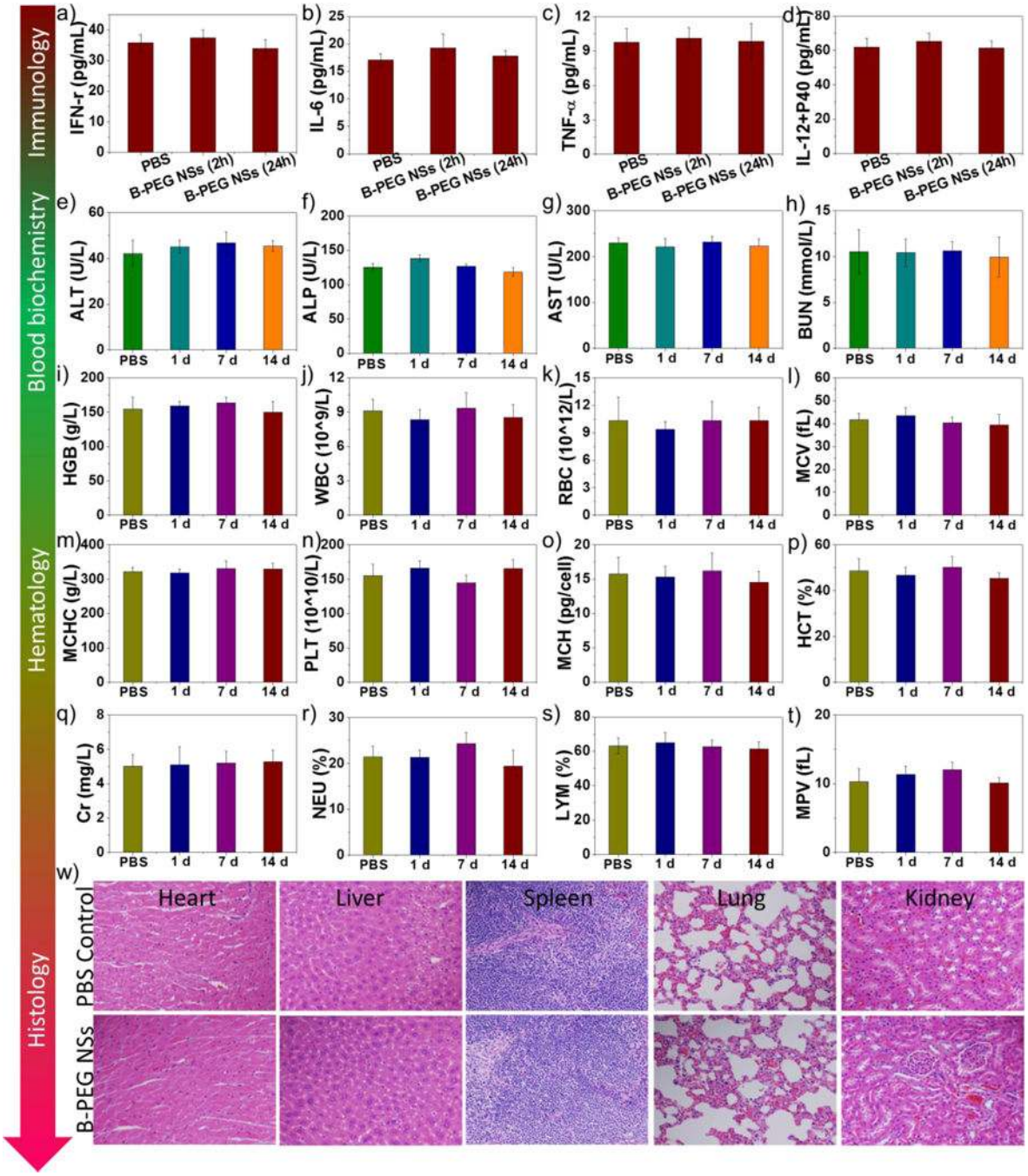

Figure 5.

In vivo toxicity evaluation. Serum levels of a) interferon-γ (IFN-γ), b) interleukin 6 (IL-6), c) interleukin-12 (IL-12+P40), and d) tumor necrosis factor-α (TNF-α) in healthy mice at 2 and 24 h after intravenous injection of PBS versus B-PEG NSs. Blood biochemistry and hematology data of Balb/c mice treated with B-PEG NSs. The data were collected at different time point after *i.v* injection: e) alanine aminotransferase (ALT), f) alkaline phosphatase (ALP), g) aspartate aminotransferase (AST), h) urea nitrogen (BUN), i) Hemoglobin (HGB), j) white blood cells (WBC), k) red blood cells (RBC), l) mean

corpuscular volume (MCV), m) mean corpuscular hemoglobin concentration (MCHC), n) platelet (PLT), o) mean corpuscular hemoglobin (MCH), p) hematocrit (HCT), q) creatinine (Cr), r) neutrophil (NEU), s) lymphocyte (LYM), and t) Mean platelet volume (MPV) levels in the blood at different time point. w) H&E stained histological images of major organs (heart, liver, spleen, lung, and kidney) from mice treated with saline versus B-PEG NSs. Images were taken under 40× objective

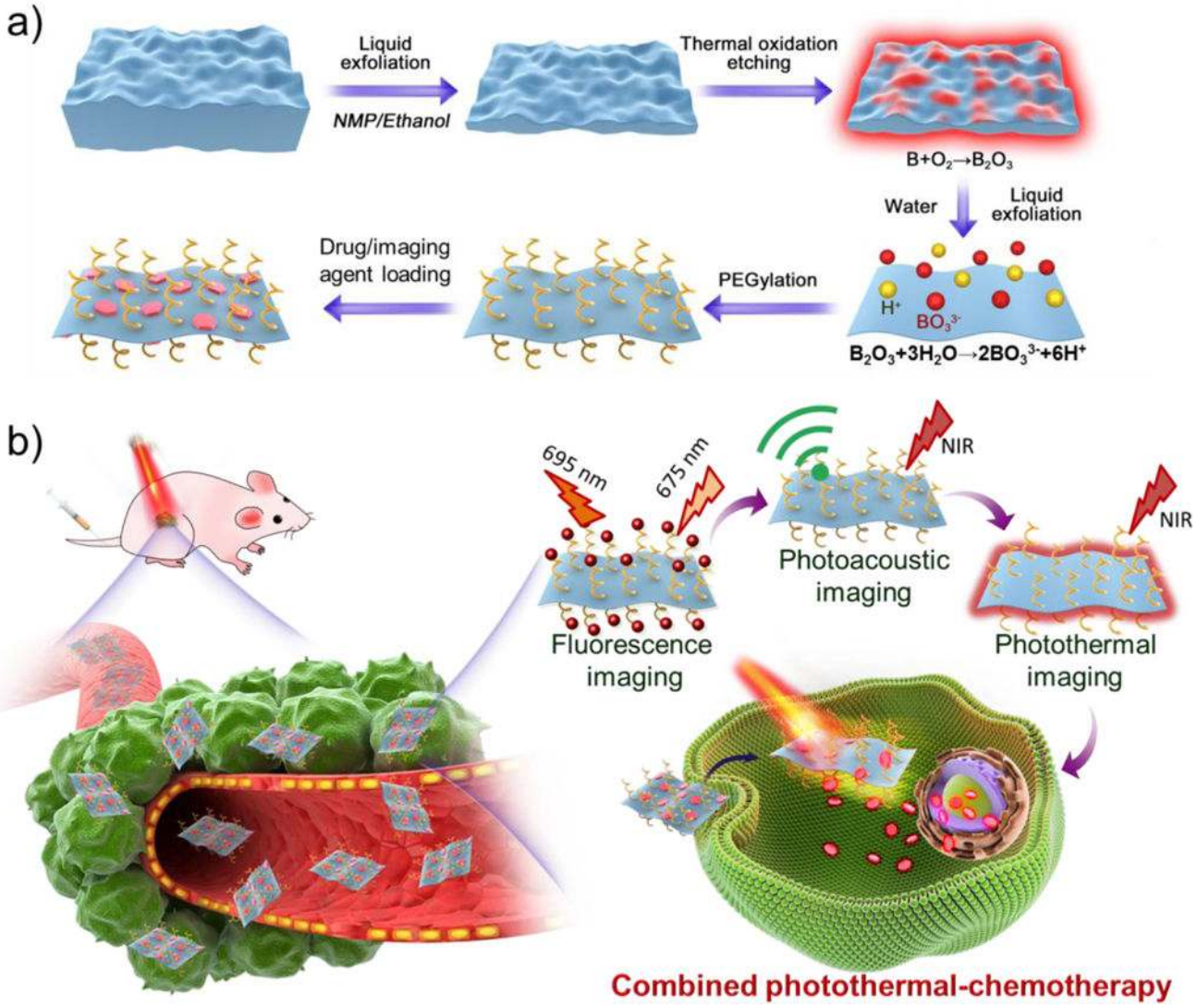

Scheme 1.

Schematic illustration of a) the preparation of 2D B-PEG/DOX NSs; and b) the systemic delivery of B-PEG/DOX NSs as a photonic nanomedicine for multimodal imaging-guided cancer therapy.